IN THE UNITED STATES PATENT AND TRADEMARK OFFICE

re Application of: D'Evelyn et al.   Examiner: W. Langel

Serial Number: 10/001,575   Filing date: Nov. 02, 2001

Docket Number: 120461-1

For: **Sintered Polycrystalline Gallium Nitride and its Production**

Mail Stop NON-FEE Amendment
Commissioner of Patents
P.O. Box 1450

Alexandria, Virginia 22313-1450

Certificate of Mailing

I HEREBY CERTIFY THAT THIS PAPER IS BEING DEPOSITED WITH THE UNITED STATES POSTAL SERVICE AS FIRST CLASS MAIL IN AN ENVELOPE ADDRESSED TO: Mail Stop NON-FEE Amendment, Commissioner of Patents, P.O. Box 1450, Alexandria, Virginia 22313-1450.

Judith Rowe   Date: August 24, 2004
Judith Rowe

DECLARATION UNDER 37 CFR § 1.132

I, Mark D'Evelyn, do hereby declare to my own knowledge that:

1.   I am currently employed as Manager of the Ceramic Processing Laboratory at the GE Global Research Center. General Electric Company ("GE") is an assignee of the above identified application.

2.   I received a B.S. degree in chemistry from UCLA in 1977, and a Ph.D. in physical chemistry from the University of Chicago in 1982. I did my postdoctoral research at Stanford University from 1982 to 1985 and at the University of Washington from 1985 to 1986.

3.   I served as an Assistant Professor of Chemistry at Rice University from 1986 to 1993, then joined the GE Global Research Center in 1993.

4.   I have over 14 years experience in superabrasive materials, synthetic diamonds, and natural diamonds, including processing of natural diamonds and synthesis of gem quality jadeite.

5.   I an inventor or co-inventor of 8 U.S. patents. I have seventy-seven (77) publications in technical journals, and twenty eight (28) publications within GE Global Research, some of which publications are made available to the public. I have published extensively on the growth and characterization of single crystal and polycrystalline materials, including 25 papers on diamond grown by chemical vapor deposition.

6   I am familiar with the issues raised in the Office Action dated February 24, 2004, including the rejectin of claims 1-6 of the patent application under 35 USC 102(b) as anticipated by, or in the alternative under 35 USC 103(a) as obvious over US Patent No. 6,113,985 of Suscavage et al.

7.   I make this declaration to provide evidence in support of the above identified patent application.

8.   It is well known that a chemical vapor deposition (CVD) process intrinsically produces textured, or non-equiaxed, material. In textured material, the crystallographic orientations of individual grains show ordering with respect to the orientation of the specimen, whereas in equiaxed material the crystallographic orientations are completely random.

9.   The mechanism for texture generation in CVD is well known. Nuclei of newly-grown material may or may not be randomly oriented. Inevitably, the growth rate in some crystallographic orientations of each nucleus will be greater than that of others, causing favorably-oriented grains to grow faster than unfavorably-oriented grains and giving rise to texture in the film.

10.   In a chemical vapor infiltration (CVI) process as disclosed in Suscavage et al., a similar texture generation process would be expected to occur in the pores of a green body during CVI, leading to texture in the densified part.

11.   I have attached herein as Exhibit A a copy of two publications supporting that texture generation would be expected to occur in the pores of a green body during CVI, thereby producing non-equiaxed parts. In the first publication [Thin Solid Films 371, 114 (2000)], Appiah and co-workers reported texture formation in SiC deposited by CVI on graphitic carbon green bodies. In the second publication [Carbon 40, 2529 (2002)], Zhang et al. observed texture formation during CVI of carbon in carbon felt green bodies.

12.   I hereby declare that all statements made herein of my own knowledge are true and that all statements made on information and belief are believed to be true; and further that these statements were made with the knowledge that willful false statements and the like so made are punishable by fine or imprisonment, or both, under Section 1001 of Title 18 of the United States Code, and that such willful false statements may jeopardize the validity of the application or any patent issued thereon.
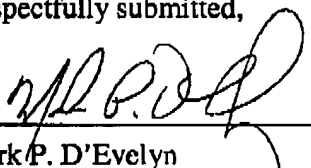
Respectfully submitted,

8/24/04
Date

Mark P. D'Evelyn

Exhibit A: Thin Solid Films 371, 114 (2000) and Carbon 40, 2529 (2002)

1-WA/1844736.6

Texturing of polycrystalline SiC films on graphitic carbon in laminated composites grown by forced-flow chemical vapor infiltration

K.A. Appiah[a], Z.L. Wang[a,*], W.J. Lackey[b]

[a]School of Materials Science and Engineering, Georgia Institute of Technology, Atlanta, GA 30332-0245, USA
[b]School of Mechanical Engineering, Georgia Institute of Technology, Atlanta, GA 30332-0245, USA

Abstract

The growth and orientation of SiC on pyrocarbon using forced-flow thermal gradient chemical vapor infiltration to deposit alternate layers of these materials has been examined by transmission electron microscopy. The SiC layers were determined to be predominantly of the cubic (β) polytype, and the close-packed $\{111\}_{SiC}$ planes were found to be mostly oriented parallel and next to the highly dense $\{0001\}_C$ basal planes of the pyrocarbon layers at the interface. A model involving close-packed plane sequencing is proposed for the C/SiC interface. © 2000 Elsevier Science S.A. All rights reserved.

Keywords: Carbides; Surface structure; Transmission electron microscopy (TEM)

1. Introduction

Silicon carbide is a versatile material possessing properties such as a wide energy band gap, high thermal conductivity, high elastic modulus and high-temperature creep resistance, which enable it to be used in a wide variety of electronic, optical and structural applications. Also, carbon, in the form of polycrystalline graphite, is well known for it is excellent thermal and electrical properties that enable its use in a variety of applications due to its anisotropic and layered structure. Carbon, when deposited as pyrocarbon by chemical vapor deposition processes, is known to exhibit varied and interesting microstructures. Thus, SiC and carbon, separately and in combination, have enormous utility in materials applications. Carbon and silicon carbide are ideally suited for use as alternate layered laminate materials due to their chemical compatibility, almost equal thermal expansion coefficients, and ease of fabrication by vapor-phase deposition methods. However, published reports on the use of carbon and SiC in combination, in spite of the enormous potential as a viable material system, are rather scarce.

Chemical vapor infiltration (CVI) is a specialized form of chemical vapor deposition (CVD) in which deposition occurs on surfaces within a porous preform, in contrast to deposition onto an external substrate surface as occurs in CVD. Thus, the thermodynamics and kinetics of the CVD process and the effects on the resulting material's microstructure are directly applicable to the CVI process. CVI is especially suited to the deposition of thin layers because it affords better control of layer thickness. In forced-flow thermal-gradient

* Corresponding author. Fax: + 1-404-894-9140.
E-mail address: zhong.wang@mse.gatech.edu (Z.L. Wang).

chemical vapor infiltration (FCVI), a thermal gradient applied to the preform coupled with the forced flow of reagents reduces total infiltration time.

In contrast to the vapor-phase nucleation and growth of single crystalline materials which has been investigated in detail and is well understood, the evolution of microstructure of polycrystalline materials has not been sufficiently elucidated. During the nucleation and growth of polycrystalline films on substrates during CVD, it has been known that the deposited material may start with nuclei of random orientations [1]. In cases where oriented columnar microstructures have been observed, they have been typically attributed to preferred growth directions, as opposed to definite orientation relationships between deposit and substrate that is characteristic of epitaxial nucleation and growth [2,3]. However, work by others [4] have shown that specific crystallographic orientation relationships, epitaxy, can occur during the polycrystalline CVD of α-SiC on β-SiC substrates. In the present work, the observed interfacial orientation relationship during the growth of polycrystalline SiC on graphitic carbon during FCVI is presented.

2. Experimental

The alternating layers of carbon and SiC were fabricated by forced-flow thermal-gradient chemical vapor infiltration of fibrous carbon preforms. Details of the FCVI fabrication process, parameters, and reactor configuration have been previously described by Lackey et al. [5]. Briefly, during the FCVI process, the reagent gases are forced to flow through the fibrous carbon preforms, and the reagent streams are altered to deposit the different matrix components alternately. The carbon layers were deposited from a mixture of propylene and hydrogen, whereas the SiC layers were deposited from a mixture of methyltrichlorosilane [MTS] and hydrogen.

Standard procedures for producing thin foils for transmission electron microscopy (TEM) examination were employed. Specimens for TEM examination were obtained by cutting ~1-mm thickness slices from a bulk sample which were then mounted in epoxy, polished, dimpled, and subsequently ion-milled to electron transparency. The ion milling was performed with argon and a rotating cold stage at a voltage of 4 kV. TEM imaging and diffraction and high-resolution TEM (HRTEM) imaging were performed using a JEOL 4000EX high-resolution microscope operating at 400 kV with a point-to-point resolution of 0.18 nm. Both bright-field and dark-field images were recorded using
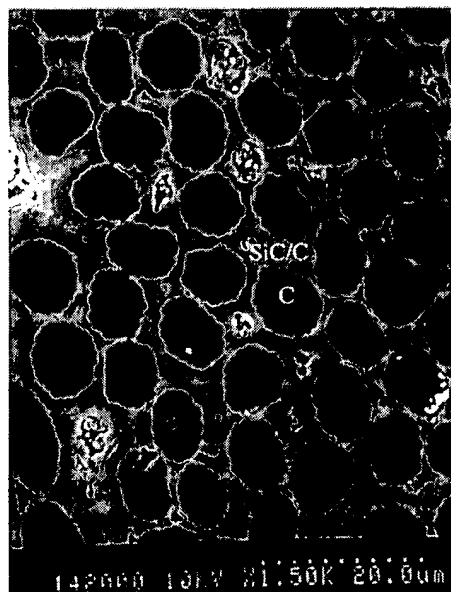

Fig. 1. SEM image showing the distribution of C–SiC layers in the laminate structure. The dark hole-shape contrast areas are the carbon fibers, and the gray contrast areas are the SiC-laminated structures grown around the carbon fibers.

an objective aperture of radius 4 mrad. HRTEM images were recorded using an objective aperture that is large enough to enclose the {0004} reflection of graphite. Scanning electron microscopy (SEM) imaging was performed using a Hitachi S800 FEG machine.

3. Results and discussion

Fig. 1 shows a SEM image of the cross-section of the laminate structure with the central carbon fiber surrounded by radial rings of alternating C and SiC layers. Fig. 2a,b are a pair of bright-field/dark-field TEM images that show the general morphology of the material with alternate layers of pyrocarbon and SiC. The dark-field image was recorded using a dominant diffraction spot indicated by a circle in Fig. 2b. The layers are seen to increase in thickness along the radial growth direction (towards the top of the images). The growth and development of the SiC crystals are evident in the dark-field image of Fig. 2b as small polycrystalline grains that grow directly on top of the carbon layers. The crystal size is seen to be anisotropic, and its length is approximately the thickness of the SiC layer. The selected area electron diffraction pattern from the indicated area in Fig. 2b suggests that the {0002}$_C$ basal planes of the pyrocarbon layer are parallel and next to the {111}$_{SiC}$ planes of the polycrystalline SiC layer. The arcs from the {0002}$_C$ reflection indicate that the basal planes have a preferred orientation as opposed to random, multiple orientations at the interface. There appears to be a specific orientation relationship, resem-
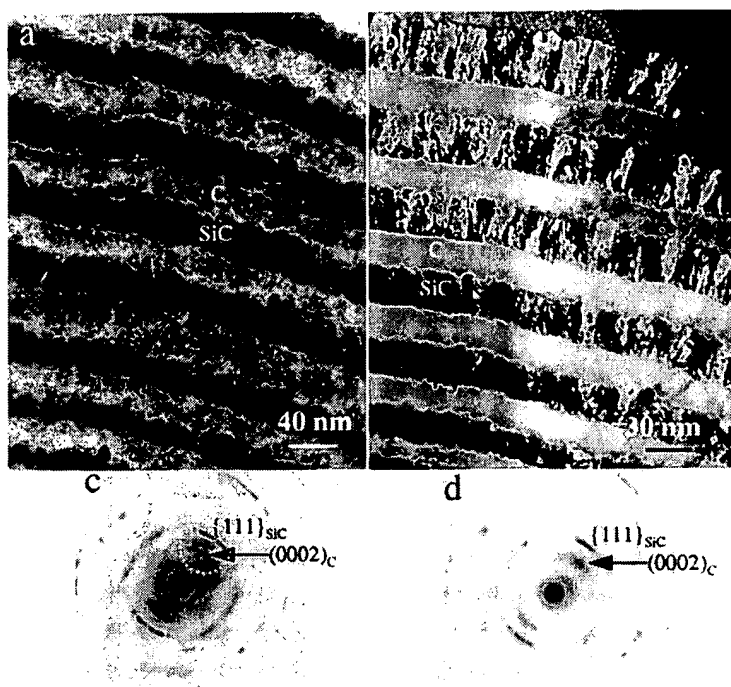
Fig. 2. (a) Bright-field TEM image showing morphology of alternate pyrocarbon and SiC layers. (b) Dark-field TEM image recorded by selecting the reflections enclosed in the circle marked in (c), showing layer morphology and crystallinity of SiC crystals. (c) Electron diffraction patterns recorded from the circled region in (b), showing the parallel orientation of (0002) pyrocarbon planes and the (111) SiC planes. (d) Another electron diffraction recorded from a different location.

bling epitaxy, at least in some localized regions, during the CVI growth of polycrystalline SiC on pyrocarbon.

Fig. 3 is a high-magnification TEM image of the carbon–SiC interface. In this image, growth of the SiC . layer occurred on the surface of the pre-existing pyro-carbon layer. It is clear from this high-magnification image that, in some regions, there appears to be a

continuity of high-density planes from the pyrocarbon to the SiC layers. This tendency of $\{0001\}_C \parallel \{111\}_{SiC}$ preserves for most of the interfacial regions, consistent with the result from the electron diffraction pattern shown in Fig. 2c, which was recorded from a much larger area. The occurrence of bands or areas which do not seem to exhibit high planar registry (Fig. 3) between
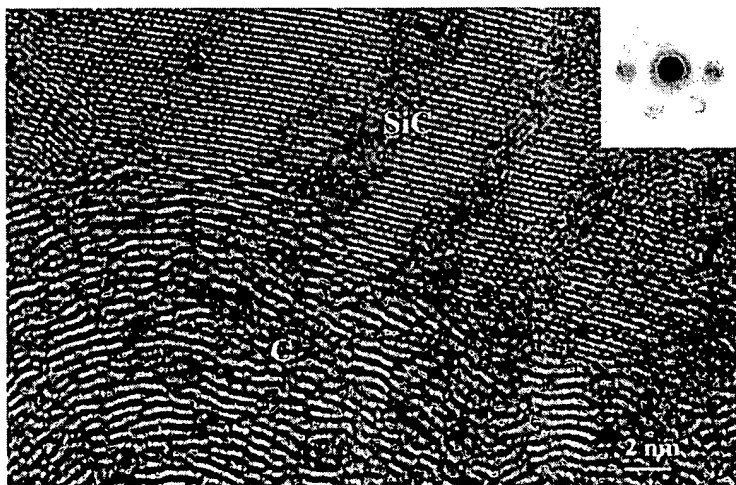

Fig. 3. High-magnification TEM image of carbon–SiC interface showing continuity of high density planes at interface; inset microdiffraction pattern reveals SiC at interface to be β polytype ($\langle 110 \rangle_{SiC}$ zone axis/$\{111\}_{SiC}$ reflections).
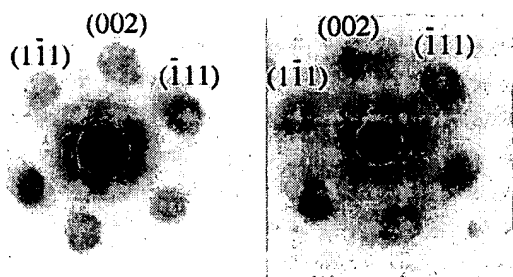
Fig. 4. Typical electron microdiffraction patterns recorded from SiC grains showing its cubic structure.

the areas of seemingly high-density plane continuity could be due to the TEM projection effect of a three-dimensional wavy interface.

The crystal structure of the SiC was determined by electron microdiffraction. Most of the microdiffraction patterns obtained from these interfacial regions were clearly identified to be of the β polytype (13 of 15 or ~ 87%). Examples of such microdiffraction patterns are shown in Fig. 4, which are indexed to be $[110]_{SiC}$ patterns of cubic SiC structure. The small number of microdiffraction patterns from these interfacial regions whose polytype could not be conclusively established appeared to be due to mixed contributions from crystals that have slightly different orientations. The close-packed $\{111\}_{SiC}$ planes of the cubic β-SiC grow directly on top of the highly dense six-membered $\{0001\}_C$ basal planes of the pyrocarbon layer.

β-SiC exhibits the zinc blende structure with inter-penetrating face-centered cubic (FCC) lattices of Si and carbon with a relative displacement of $1/4 [111]_{SiC}$, or, alternatively, a lattice with Si atoms at the fcc positions and carbon atoms occupying one-half of the tetrahedral locations. Thus, the close-packed {111} planes can be viewed as a double layer of Si and carbon atoms, as shown in Fig. 5a. The β-SiC $\{111\}_{SiC}$ planes follow a stacking sequence of ABCABC... The stacking parallel to the basal plane for graphite can be represented by the A'B'A'B'... stacking sequence of the $\{0001\}_C$ planes as shown in Fig. 5b.

The parallel alignment of close-packed planes in the C-SiC system could be explained by considering a simple model of the possible stacking sequence of the close-packed planes at the interface. If the pyrocarbon layer maintains the basal plane at the surface, the next layer of β-SiC $\{111\}_{SiC}$ close-packed planes could easily continue the stacking sequence by occupying the A', B' or C' stacking position (see Fig. 5c), or either of two available positions not occupied by the terminating pyrocarbon layer. The β-SiC $\{111\}_{SiC}$ planes could then easily continue to maintain the ABCABC... stacking sequence characteristic of the cubic close-packed structure. The first contacting layer of β-SiC with C can be either Si or C atoms depending on the energetics of the

particular bonding scenario. Such a texturing orientation is likely to exist even at the very first layer of SiC because the carbon fibers at the center tend to have the graphitic layers parallel to the outer surface of the fiber. In this work, such parallel alignment of graphite layers at contacting surfaces may be particularly conducive to the nucleation of SiC $\{111\}_{SiC}$ planes.

Despite the increasing basal plane alignment of the pyrocarbon layer towards the interface, the structure still remains turbostratic and deviant from that of highly crystalline graphite. Crystals of graphite, particularly those deposited from vapor-phase processes are known to exhibit various degrees of preferred orientation of basal planes [6-8] and are mostly turbostratic at low
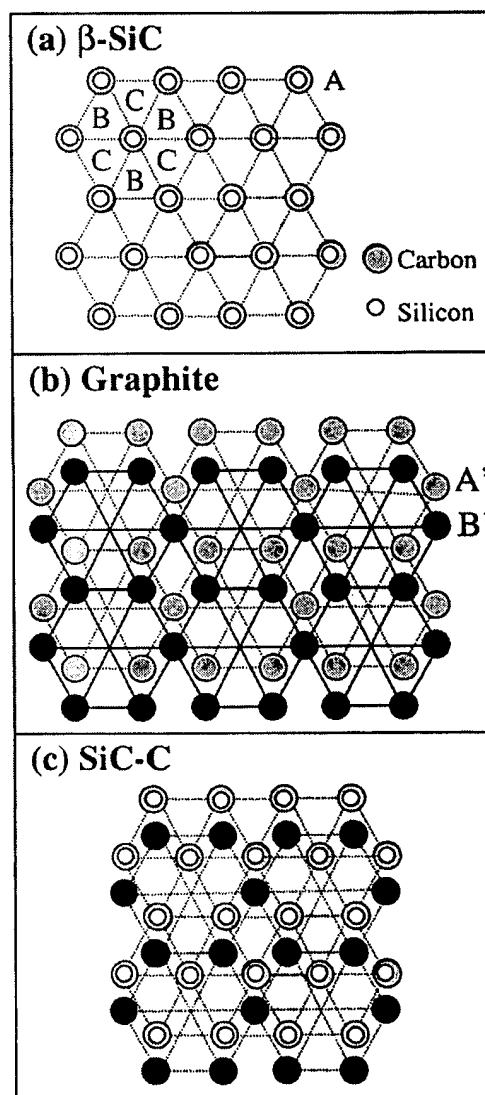

Fig. 5. (a) Model of the ideal stacking sequence of ABCABC... parallel to the β-SiC (111) planes. (b) Model of the ideal stacking sequence, A'B'A'B'..., parallel to the graphite (0001) basal planes. (c) Model of the stacking of high-density planes at the C-SiC interface.

temperatures (approx. 1170 K, similar to the deposition temperature employed in this work). Coupled with the fact that the alternating layers of carbon and SiC are deposited as concentric circles (see Fig. 1), thus introducing some amount of inherent curvature to the interface, it is conceivable that the carbon basal planes would be particularly oriented for favorable nucleation of SiC $\{111\}_{SiC}$ planes only at certain locations. Once nucleation is initiated in these favorable regions, continual growth of the SiC is assured through the layer thickness, hence the array of SiC $\{111\}_{SiC}$ planes emanating from the carbon layer. The SiC grain tends to grow along the radial direction, but the lateral grain size is strongly affected by the curvature of the SiC layer. The dark-field image given in Fig. 2b indicates that the lateral grain size increases with the increase of the radial distance from the central region. This is understandable because the curvature of the layer can be accommodated by the rotation of the grains and the rotation angle increases with a decrease in the radial distance, possibly leading to smaller lateral size.

At the pyrocarbon–SiC interface, the close-packed $\{111\}$ SiC planes can be stacked on top of the graphite basal planes, such that the $\langle -1\,1\,0\rangle_{SiC}$ close-packed direction is parallel to the $\langle 1\,1\,-2\,0\rangle_C$ direction in the graphite basal plane. Along the close-packed direction in the SiC $\{111\}$ plane, the interatomic distance is calculated to be ~0.308 nm. In the graphite basal planes, the C–C distance is 0.142 nm for nearest neighbors and 0.246 nm for second nearest neighbors. The lattice mismatch, f, was calculated as $d_{SiC}/d_C - 1$, where d_{SiC} and d_C are the interatomic distances along the pertinent directions in SiC and graphite (second nearest neighbor), respectively. Thus, the calculated lattice mismatch along the $\langle -1\,1\,0\rangle_{SiC} \parallel \langle 1\,1\,-2\,0\rangle_C$ direction is found to be quite large: approximately 0.25. Although the materials were deposited at ~1150 K, the thermal expansion effects were not considered in the mismatch calculations because they are not expected to significantly alter the results.

In view of the substantial lattice mismatch and dissimilar crystal structures of the pyrocarbon and SiC layers, some level of localized epitaxy seems to exist at all in this polycrystalline system. Epitaxy has been observed in some systems despite large differences in lattice parameters and crystalline structures such as AlN on Al_2O_3 [9] and CdTe on GaAs [10]. It is believed

that localized epitaxy can occur on the individual grains of a polycrystalline substrate, and, furthermore, face-centered cubic (fcc) and hexagonal close-packed (hcp) systems have been known to allow epitaxy on $\{111\}_{SiC}$ and $\{0001\}_C$ planes respectively [10]. Such a scenario would be consistent with the apparent localized epitaxy of SiC on graphitic carbon observed in this work. In this work, certain grains of the polycrystalline SiC, namely grains that present $\{111\}_{SiC}$ planes, seem to adopt an epitaxial relationship on the $\{0001\}_C$ graphitic basal planes.

In summary, alternating layers of pyrocarbon and SiC were deposited by the FCVI process, and the interface between pyrocarbon and SiC layers were investigated. In some localized areas, there appeared to be a definite orientational relationship between the pyrocarbon layers and the crystalline grains of the SiC layers. In particular, high-magnification TEM and diffraction revealed that highest-density planes seemed to be continuous from the $\{0001\}$ basal planes of the pyrocarbon layer to the close-packed $\{111\}$ planes of β-SiC. A simple model of close-packed plane stacking sequence at the interface was proposed and appeared to be consistent with the interfacial observations.

Acknowledgements

References

[1] J.L. Kenty, J.P. Hirth, Surf. Sci. 15 (1969) 403.
[2] A. van der Drift, Philips Res. Rep. 22 (1967) 267.
[3] E.A. Matson, S.A. Polyakov, Phys. Status Solidi A 41 (1997) K93.
[4] B.W. Sheldon, T.M. Besmann, K.L. More, T.S. Moss, J. Mat. Res. 8 (1993) 1086.
[5] W.J. Lackey, S. Vaidyaraman, K.L. More, J. Am. Cer. Soc., 1 80 (1997) 113.
[6] J.D. Buckley, D.D. Edie, Carbon–Carbon Materials and Composites, Noyes Publications, New Jersey, 1993.
[7] A.S. Johansson, J. Lu, J.O. Carlsson, Thin Solid Films 252 (1994) 19.
[8] J. Bokros, in: P.L. Walker (Ed.), Chemistry and Physics of Carbon, 5 (1969) 1.
[9] F.A. Ponce, D.P. Bour, Nature 386 (1997) 351.
[10] D.L. Smith, Thin Film Deposition: Principles and Practice, McGraw-Hill Press, New York, 1995.

Chemical vapor infiltration of carbon fiber felt: optimization of densification and carbon microstructure

W.G. Zhang, Z.J. Hu, K.J. Hüttinger*

Institut für Chemische Technik, Universität Karlsruhe, Kaiserstr. 12, D-76128 Karlsruhe, Germany

Abstract

A carbon fiber felt with a fiber volume fraction of 7.1% was infiltrated at temperatures of 1070 and 1095 °C and methane pressures from 5 to 30 kPa to confirm the inside–outside densification derived from model studies with capillaries 1 mm in diameter. Bulk densities and residual open porosities were determined as a function of infiltration depth at various heights of the felt. The texture of the infiltrated carbon was studied by polarized-light microscopy and characterized with the aid of the extinction angle. Inside–outside densification was demonstrated up to the maximum pressure of 30 kPa at 1070 °C and up to 13.5 kPa at 1095 °C, leading to bulk densities above 1.9 g/cm^3. A pure, high-textured carbon matrix is formed in the pressure range from 9.5 to 11 kPa at 1095 °C. At lower and higher methane pressures and lower temperature, a less textured carbon is formed. The results are based on the growth mechanism of carbon deposition. They strongly support recent conclusions that high-textured carbon is formed from a gas phase exhibiting an optimum ratio of aromatic hydrocarbons to small linear hydrocarbons, preferentially ethine. This model is called the particle-filler model. Aromatic hydrocarbons are the molecular particles and small linear hydrocarbons are the molecular filler, necessary to generate fully condensed planar structures.
© 2002 Elsevier Science Ltd. All rights reserved.

Keywords: A. Pyrolytic carbon; B. Chemical vapor infiltration; C. Mercury porosimetry, Optical microscopy; D. Microstructure

1. Introduction

Isobaric, isothermal chemical vapor infiltration (CVI) is the accepted process for the production of carbon reinforced carbon used in the aerospace industry (rocket and missile nozzles, brake disks). Since its development in the 1960s, this process has been considered to be strongly diffusion limited [1,2]. To overcome this problem, low infiltration rates and, especially, very low pressures are recommended and have been used [1,2]. Several special processes, such as temperature and pressure gradients, and forced and pulsed flow processes, have been investigated [1,2], but did not replace the classical isobaric, isothermal CVI process for mass production, for example of brake disks for aircraft brakes.

In 2000 and 2001 it was shown for the first time by

experimental studies [3,4] as well as numerical simulations [5] that the infiltration profiles may increase from the surface to the center of a porous preform. In other words, they do not necessarily decrease as is the case in a diffusion-limited infiltration process. The above studies were based on the infiltration of capillaries, 1 mm in diameter and up to 50 mm in length.

Cylindrically shaped capillaries, in particular with a relatively large diameter, are presumably not representative of a porous structure, for example a carbon fiber preform used to produce carbon fiber reinforced carbon. Independent of the fiber architecture, a carbon fiber preform exhibits a much larger surface area/volume ratio, which has a significant influence on the deposition chemistry and kinetics [6,7]. Therefore, it was the first goal of this study to reproduce and confirm the above results [3–5] by infiltration of a carbon fiber structure.

For industrial and, in particular, aerospace applications of carbon fiber reinforced carbon, a matrix with a high-textured carbon is required, but most of the results presented in the literature show a change of texture with

---

*Corresponding author. Tel.: +49-721-608-2114; fax: +49-721-608-4820.

E-mail address: huettinger@ict.uni-karlsruhe.de (K.J. Hüttinger).

progressive infiltration, usually from low- or medium-textured to high-textured [8–11]. The second goal of this study was to develop a model correlating carbon formation chemistry with carbon texture, which can be determined by various means [12]. As little is known about the chemistry of carbon formation, use was made of its analogy to mechanisms of aromatic growth [13]. A model of carbon formation is required to produce carbon fiber reinforced carbon with a well-defined, desired texture of the carbon matrix. Available models [14–18] are incomplete or not applicable to CVI for various reasons.

Development of the model is based on the surface area/volume ratio [15], according to which low- or medium-textured carbon, deposited in the initial stage of infiltration, is formed from large species (aromatic and/or polyaromatic hydrocarbons). The transition to medium- and high-textured carbon, occurring with progressive infiltration, is attributed to an increase of the surface area/volume ratio, which causes a shift of the carbon formation chemistry from large to smaller species (linear hydrocarbons). Other models based on chemical vapor deposition (CVD) as well as CVI studies correlate large species with high-textured carbon and small species with medium-textured carbon [14,16]. The reasons for these different conclusions will be discussed below.

The experimental investigations were performed using a carbon fiber felt as a fiber preform. This felt was infiltrated at temperatures of 1070 and 1095 °C, and methane pressures ranging from 5 to 30 kPa. Additional experiments were performed using methane–hydrogen mixtures instead of pure methane. Density and pore size distributions as a function of infiltration depth were determined for analysis of the infiltration profiles. The texture of the infiltrated carbon was characterized using the extinction angle, A_e, determined by polarized-light microscopy [19,20].

2. Experimental

2.1. Infiltration experiments

A scheme of the infiltration reactor is presented in Fig. 1. The felt (4) is fitted into a cylindrically shaped sample holder (5). With the aid of the sample holder the gas flow is limited to a narrow annulus, about 2 mm in width (gap reactor). Short residence times of the gas, which are extremely important [4,5], can thus be achieved with moderate volume flows. The dimensions of the rectangular-shaped felt are 42 mm (length)×16 mm (width)×40 mm (height). According to the length of the felt, the infiltration depth amounts to 21 mm, if infiltrated from both sides (as shown in Fig. 1). In a single case, one side of the felt was sealed to increase the infiltration depth to 42 mm.

The felt was procured from Conradty (Nürnberg, Ger-

1. gas outlet
2. hole for thermocouple
3. graphite foil
4. felt
5. sample holder (graphite)
6. gap for gas flow
7. hole for thermocouple
8. ceramic tube (Pythagoras®)
9. space holder
10. fitting (graphite)
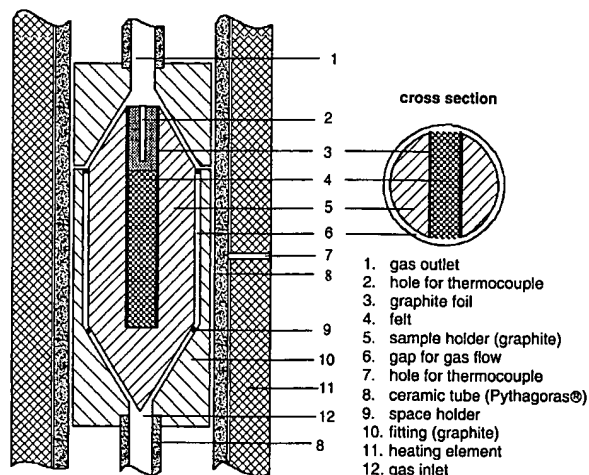11. heating element
12. gas inlet

Fig. 1. Schematic drawing of the infiltration reactor.

many). It was not high-temperature treated. The fiber volume fraction was 7.1% and the fiber density 1.72 g/cm³.

The gas flows from the bottom to the top. The residence time at a given temperature and pressure is determined for the cylindrical part of the annulus 40 mm in height; a volume change caused by decomposition of methane is not considered. Heating to the infiltration temperature is performed in flowing pure argon. Temperature is controlled on top of the felt (not shown in Fig. 1). After reaching the desired temperature the thermocouple is removed to avoid closing of the narrow outlet tube during infiltrations of several days. Finally, infiltration is started with the desired methane flow.

2.2. Preparation of samples and analytical methods

Infiltrated felts were cut into 16 samples as shown in Fig. 2. The bulk density was determined for all samples. The pore size distribution was studied using mercury porosimetry. For this purpose a set of two samples had to be used, samples 2A and 3A for the outer region ('surface') and samples 2B and 3B for the inner region ('center'). Mercury porosimetry yields further important parameters such as bulk density, skeletal density, cumulative pore volume and surface area. With these data the density of the infiltrated carbon (matrix density) can be determined:

$$\rho_{matrix} = \frac{\rho_{bulk} - \delta_F \cdot \rho_{fiber}}{\rho_{bulk} - \delta_F \cdot \rho_{skeleton}} \cdot \rho_{skeleton} \qquad (1)$$

where ρ_{matrix}, ρ_{bulk} and $\rho_{skeleton}$ are the matrix, bulk and skeletal density, respectively. ρ_{fiber} and δ_F are the density of the carbon fiber and its volume fraction, 1.72 g/cm³ and 7.1%, respectively.
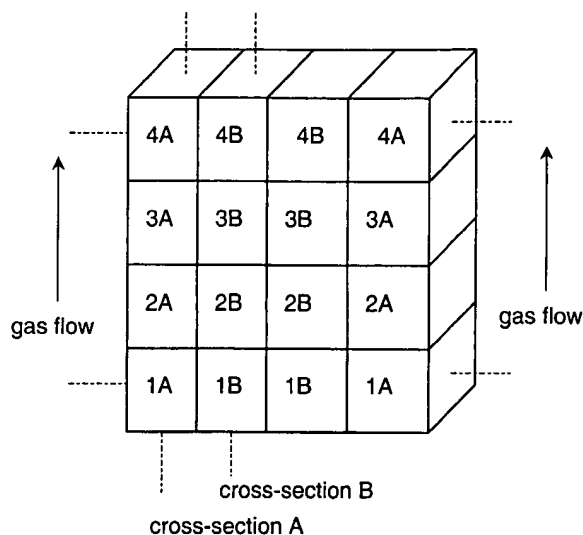
Fig. 2. Scheme showing the preparation of samples from an infiltrated block.

Fig. 3. Bulk density as a function of the distance from the center of the felt at various heights: (□) 5 mm; (O) 15 mm; (∇) 25 mm; (△) 35 mm. Infiltration conditions: 1070 °C and 20 kPa CH$_4$, $\tau = 0.1$ s, $t = 120$ h.

Additionally, the surface area/volume ratio at various stages of infiltration (densification) can be determined using

$$[A/V] = \frac{\text{cumulative pore surface area per gram}}{\text{cumulative pore volume per gram}} \qquad (2)$$

The microstructure was studied with polarized-light microscopy (PLM) at cross-sections A and B as shown in Fig. 2. For a quantitative description of the carbon texture the extinction angle, A_e, was determined [12,19]. In the case of a completely circular fiber cross-section the error is about ±1°. Because the fibers in the felt are not really circular (see below) the error is in the range of ±1.5°.

3. Results

3.1. Densification

Infiltration experiments were performed at both temperatures, 1070 and 1095 °C, methane pressures from 5 to 30 kPa and with two methane–hydrogen mixtures at the same residence time of 0.1 s and the same infiltration time of 120 h. Typical bulk density profiles at various heights in the felt, obtained by infiltration from both sides, are shown in Fig. 3. A density increase from the surface to the center, indicative of an increase of the deposition rate, is in agreement with the model studies [3–5]. The lower density gradients in the upper part of the felt result from the advanced state of the gas-phase reactions (pyrolysis) of the methane as it flows along the felt surface. The same result was obtained with capillaries [4,5].

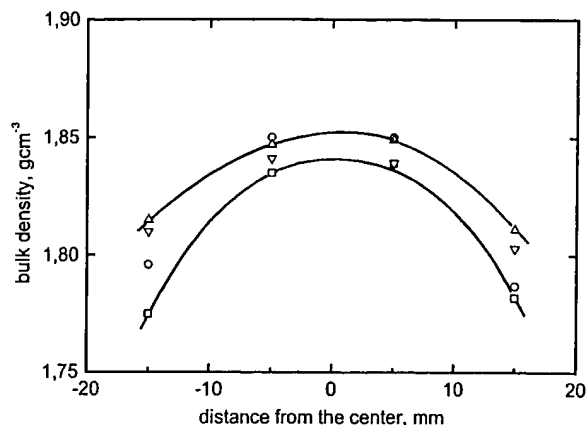Density profiles obtained under the same conditions, but

with infiltration from one side, are given in Fig. 4, which shows that the sealed end of the felt is completely densified to a remarkably high density of about 1.92 g/cm^3. This high density, combined with a strong density decrease towards the surface, confirms a major conclusion from the model studies: increasing infiltration depths may be advantageous for improving densification [4,5]. According to the revised CVI model, this results from a stronger increase of the deposition rate from the surface to the interior at larger infiltration depths [3–5].

A density increase from the surface to the center of the felt was generally obtained at the lower temperature of 1070 °C (all pressures), and at lower pressures (up to 13.5 kPa) at the higher temperature of 1095 °C. The results are summarized in Figs. 5 and 6. These figures show profiles of average bulk densities, neglecting the influence of
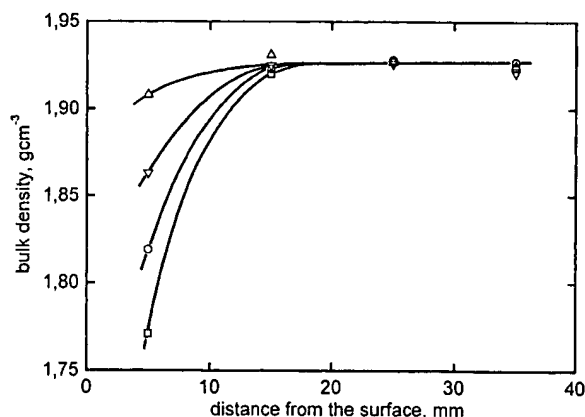

Fig. 4. Bulk density as a function of the distance from the surface of the felt (infiltration from one side) at various heights (see Fig. 3). Infiltration conditions: 1070 °C and 20 kPa CH$_4$, $\tau = 0.1$ s, $t = 120$ h.
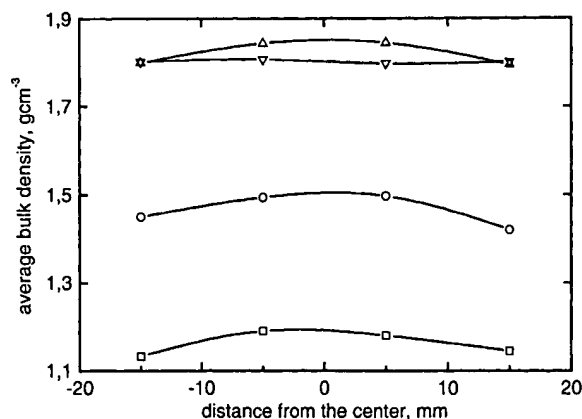
Fig. 5. Average bulk density as a function of the distance from the center of the felt for various methane pressures: (□) 5 kPa; (○) 10 kPa; (△) 20 kPa; (▽) 30 kPa. Infiltration conditions: 1070 °C, $\tau = 0.1$ s, $t = 120$ h.

height, for equal infiltration times. The density profiles slightly decrease from the surface to the center at 1095 °C and pressures of 20 and 30 kPa. Density differences from the surface to the center of less than 3 to 5% are not sufficient to indicate a decisive diffusion limitation, especially in consideration of such unusually high pressures.

The bulk density is a global property resulting from a complexity of influences. At a constant fiber volume fraction, it is determined by the real density of the matrix, closed and residual open porosity. Therefore, pore size distributions were additionally determined. Typical results are given in Figs. 7 and 8. These figures show the cumulative volume of open pores up to a pore entrance diameter of 3 nm for infiltrations at a temperature of 1070 °C and a pressure of 20 kPa (Fig. 7) as well as at 1095 °C and pressures of 10 kPa (Fig. 8a) and 20 kPa (Fig. 8b).
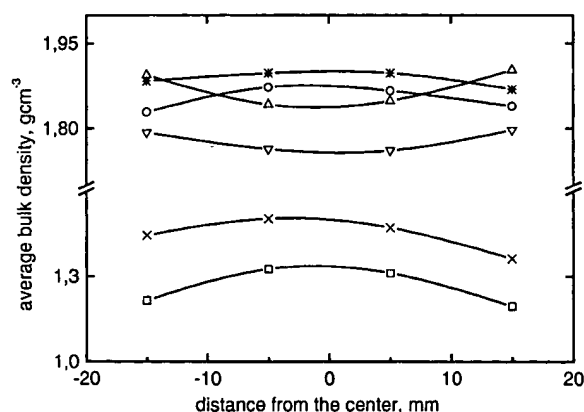

Fig. 6. Average bulk density as a function of the distance from the center of the felt for various methane pressures: (□) 5 kPa; (×) 7.5 kPa; (○) 10 kPa; (*) 13.5 kPa; (△) 20 kPa; (▽) 30 kPa. Infiltration conditions: 1095 °C, $\tau = 0.1$ s, $t = 120$ h.
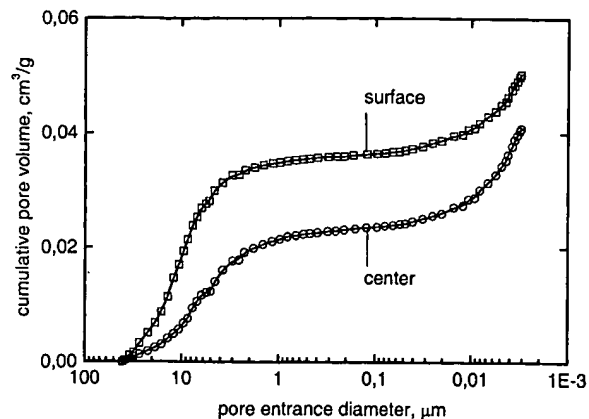

Fig. 7. Cumulative pore volume as a function of pore entrance diameter of felt infiltrated at 1070 °C and 20 kPa CH_4.

Results obtained for all investigated samples are summarized in Table 1. Separate values are given for the pore volumes of the outer region ('surface': average value of samples 2A and 3A) and the inner region ('center': average value of samples 2B and 3B). A distinction between the total volume of the residual open porosity up to pore diameters of 1 μm and 3 nm is made because pore
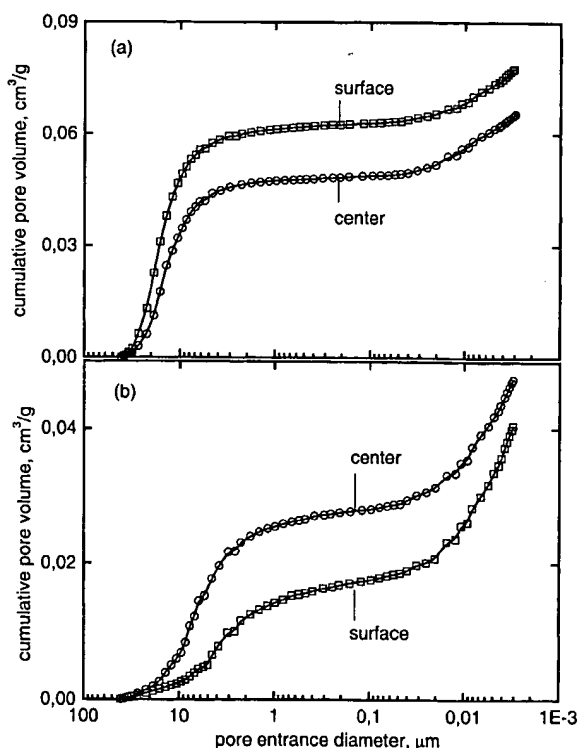

Fig. 8. Cumulative pore volume as a function of pore entrance diameter of felt infiltrated at 1095 °C, 10 kPa (a) and 20 kPa CH_4 (b).

size distributions in Figs. 7 and 8 suggest that pores smaller than 1 μm in diameter are difficult to fill at longer infiltration times. A comparison of results of Figs. 7 and 8 as well as the data of Table 1 with the bulk densities of Figs. 5 and 6 shows that a density increase from the surface to the center corresponds to a lower open pore volume in the center compared to the surface, and vice versa.

Using Eq. (1), relating the value of the fiber volume fraction and the fiber density as well as the bulk and skeletal density of the infiltrated felt, the density of the carbon matrix was estimated. Because this estimate does not consider closed pores and open pores smaller than 3 nm, the resulting values represent a lower limit.

The results for both temperatures are presented in Fig. 9. This figure shows the average matrix densities of samples 2B and 3B (center) as a function of methane pressure. Methane pressure has a significant influence; a maximum density of about 2.15 g/cm^3 at 1095 °C and 11 kPa indicates a high-textured carbon, which is obviously obtained at neither lower nor higher pressures. The influence of pressure at 1070 °C is similar, but the densities are lower over the total range of pressures.

Results obtained at a methane pressure of 20 kPa and hydrogen additions of 4 and 10 kPa are presented in Fig. 10 and Table 2. With pure methane (Fig. 10, filled symbols) the bulk density decreases slightly from the surface to the center, indicating the onset of diffusion limitation. The addition of hydrogen produces a bulk density increase from the surface to the center, implying that there is no diffusion limitation, even though the total pressure was increased from 20 kPa to 24 and 30 kPa. The lower bulk densities obtained with 10 kPa hydrogen, compared to 4 kPa, demonstrate the inhibiting effect of hydrogen on the deposition rate. Matrix densities as a function of hydrogen partial pressure determined using Eq. (1) are shown in Fig. 11. Hydrogen addition effects a
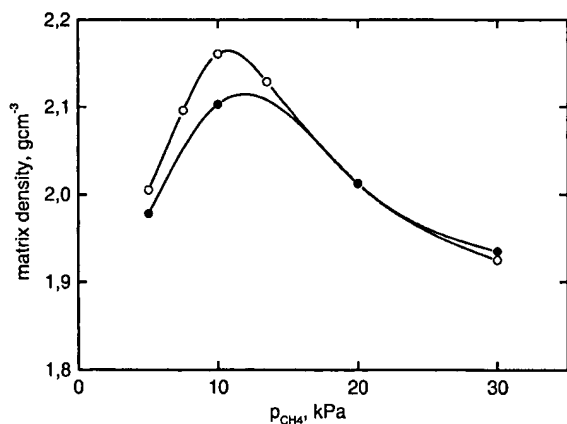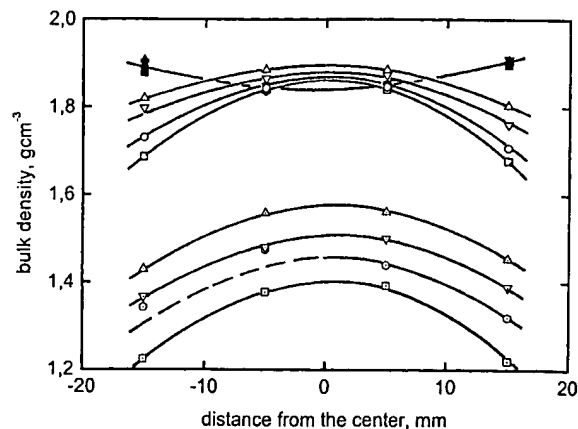

Fig. 10. Bulk density as a function of the distance from the center of felt infiltrated at 1095 °C using 20 kPa CH_4 (filled symbols), 20 kPa CH_4 + 4 kPa H_2 (open symbols) and 20 kPa CH_4 + 10 kPa H_2 (open symbols with dot) at various heights (see Fig. 3).

density increase in the center up to about 6 kPa, but simultaneously a continuous decrease of density at the surface at increasing hydrogen partial pressures.

3.2. Microstructure

The microstructure of the matrix carbon was investigated for all cross-sections 1A to 4A and 1B to 4B (see Fig. 2) using polarized-light microscopy. The observed microstructures vary in most cases not only from bottom to top (1 to 4), but also from surface to center (A to B). The micrographs shown correspond to cross-sections 1A and 4B, exhibiting the most pronounced textural differences of the matrix carbon.

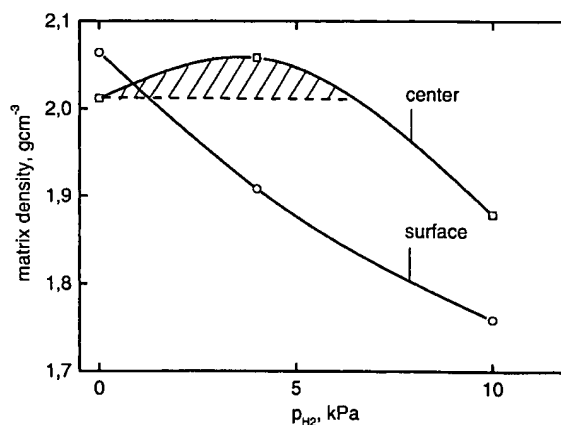The microstuctures obtained for increasing methane pressures at 1070 °C are shown in Fig. 12. At 5 kPa, a

Fig. 9. Matrix density of felt as a function of methane pressure infiltrated at 1070 °C (●) and 1095 °C (○).

Fig. 11. Matrix density of felt as a function of hydrogen partial pressure infiltrated at 1095 °C using 20 kPa CH_4 and CH_4–H_2 mixtures.

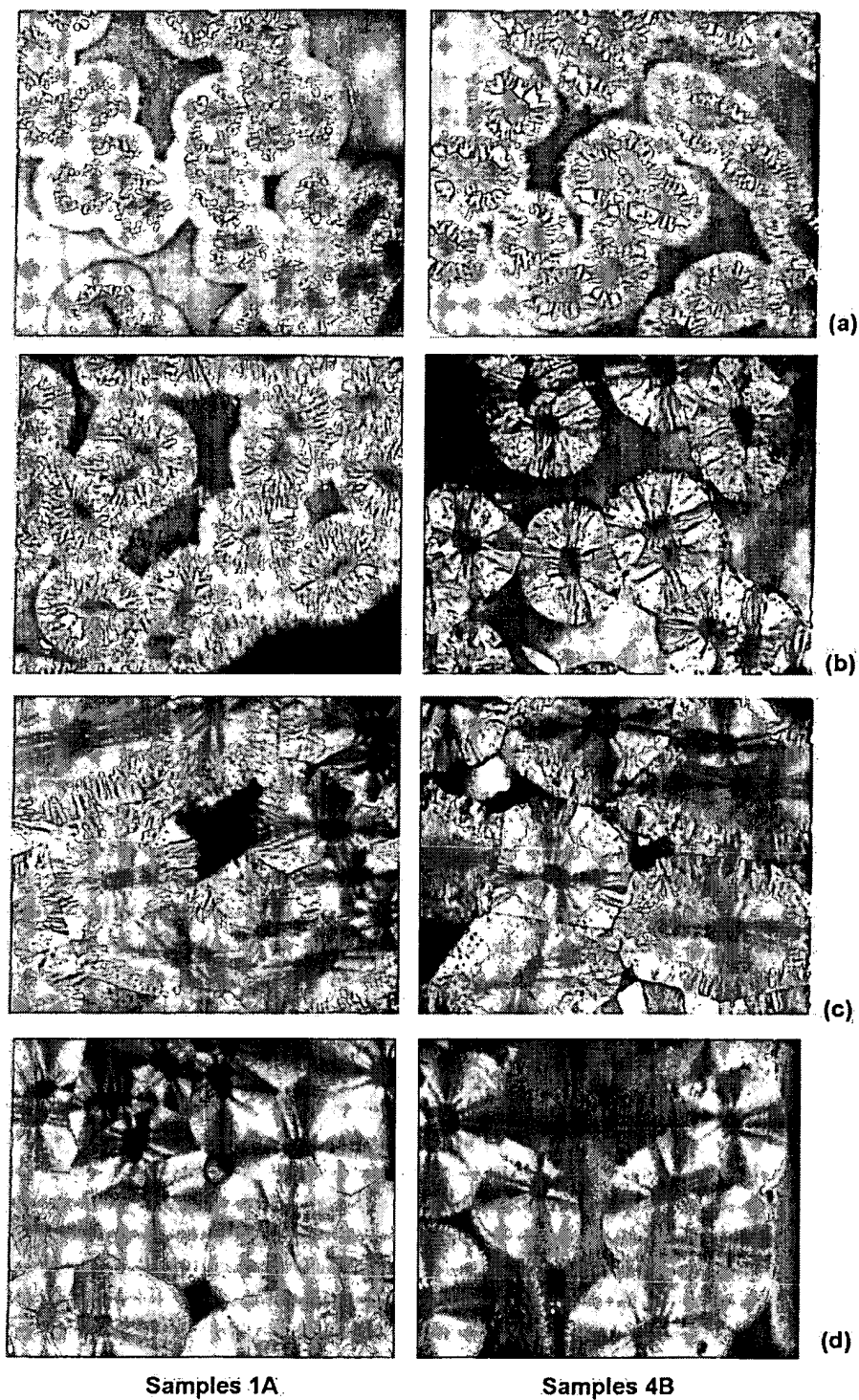**Samples 1A**   **Samples 4B**

Fig. 12. Microstructure of samples 1A and 4B from infiltrations at 1070 °C and methane pressures of 5 (a), 10 (b), 20 (c) and 30 kPa (d). Magnification 500×: 1 mm corresponds to 2 μm.

medium-textured carbon layer is followed by a low-textured layer (a). A pressure increase to 10 kPa effects a dramatic change in cross-section 4B, showing a single layer of high-textured carbon (b). At still higher methane pressures of 20 and 30 kPa, cross-section 1A displays a single layer of medium-textured carbon (c, d), which is also observed at cross-section 4B, but only at 30 kPa (d).

Results obtained for 1095 °C are compiled in Fig. 13. The textures at 5 kPa are similar to those at 1070 °C (a). At 10 kPa methane pressure a single layer of high-textured carbon is formed (b). A similar result is obtained at 13.5 kPa (c), except for a very thin sub-layer of medium-textured carbon in cross-section 4B. At 20 kPa (see Fig. 14a), two layers are again formed resulting from a transition from medium- to high-textured carbon. A further pressure increase to 30 kPa (d) favors the deposition of medium-textured carbon, as already observed at 1070 °C.

Microstructures obtained for 20 kPa methane pressure and methane/hydrogen mixtures are shown in Fig. 14. Addition of 4 kPa hydrogen does not significantly change the texture of the first and the second layer deposited in cross-section 4B (compare Fig. 14a and b), but the thickness of the first low-textured layer is clearly reduced. A similar effect of hydrogen can be observed in cross-section 1A, although the thickness of the first layer is only slightly decreased. Addition of 10 kPa hydrogen causes a dramatic texture change (Fig. 14c). A very thin and diffuse layer of extremely low-textured carbon in both cross-sections is followed by a second layer showing very weak extinction.

The extinction angle, A_e, was used for quantitative characterization of the various textures. The results for depositions with pure methane are presented in Figs. 15 (1070 °C) and 16 (1095 °C). These figures show two bands of extinction angles essentially determined by the lowest angle (sample 1A) and the highest angle (sample 4B). The ranges of extinction angles corresponding to high- (HT), medium- (MT) and low-textured carbon (LT) are shown by dashed-dotted lines [12].

The influence of pressure on the extinction angle of both the first and the second layers is similar at both temperatures, but the value of the extinction angles at 1095 °C compared to 1070 °C is clearly higher. A maximum in the extinction angle and thus the highest texture exists between 10 and 15 kPa methane pressure at both temperatures. Lower extinction angles at lower and higher pressures indicate the deposition of less textured carbon. It is even more remarkable that a single layer is formed at 10 kPa at both temperatures. Therefore, these angles imply an intersection point with decisive consequences. A transition from the first to the second layer leads to an improved texture (higher A_e) at increasing pressures and a worse texture (lower A_e) at decreasing pressures. Based on these results a chemical model of carbon formation is presented in Section 4.3. From a practical point of view it is noteworthy that a carbon fiber reinforced carbon with a

pure high-textured matrix carbon can be produced at 1095 °C and pressures ranging from about 9.5 to 11 kPa (Fig. 16). In this pressure range the extinction angles are greater than 18°. The different extinction angles between 18 and 24° for the first and second layer may be attributed to a texture change within a single high-textured layer. Such a change is not detectable with polarized light because it produces an integral or average value of the total layer [20].

A matrix of pure high-textured carbon is not achieved at 1070 °C. The results of Fig. 15 indicate the possibility of producing a pure medium-textured matrix at a methane pressure of about 17 kPa and a pure low-textured matrix at pressures above 26 kPa.

For infiltrations at 1095 °C the average thickness of the first layer was determined at cross-sections 1A and 4B (Fig. 17). In the low-pressure regime from 0 to about 10 kPa methane pressure the layer thickness at both cross-sections shows a sharp increase. In the pressure range from about 9.5 to 11 kPa a single layer of pure high-textured carbon is obtained at both cross-sections (Fig. 16). At pressures above 11 kPa, two layers are again formed, with the thickness of the first layer strongly increasing with increasing methane pressure (high-pressure regime).

In both pressure regimes the layer thickness in cross-section 4B (center) is greater than that in cross-section 1A (surface). The inverse situation at the highest pressure of 30 kPa may be attributed to a diffusion limitation, indicated by the bulk densities in Fig. 6 and porosities in Table 1. In the low-pressure regime, the increasing layer thickness corresponds to an improved texture, in the high-pressure regime to a worse texture (Fig. 16).

4. Discussion

4.1. Densification

Model studies [3–5] have shown that densification of a porous structure may occur from the center to the surface (inside–outside densification) provided that the residence time of the gas in the space surrounding the porous structure is sufficiently short to prevent significant methane decomposition. Additionally, it has been shown that increasing pressure and infiltration depth are advantageous, not only to accelerate the densification process, but also to favor inside–outside densification. This is plausible considering that the process is not determined by diffusion of methane into the structure, but by the outward diffusion of larger hydrocarbons formed in the porous structure (because of the extended residence time) [21].

Bulk densities, used as a rough measure to characterize densification, confirm inside–outside densification, at 1070 °C up to 30 kPa and at 1095 °C up to 13.5 kPa (Figs. 3, 5 and 6). The beneficial effect of increased infiltration depth follows from a comparison of the results of Figs. 3 and 4.